



Long-term oxidation behavior of spinel-coated ferritic stainless steel for solid oxide fuel cell interconnect applications

J.W. Stevenson*, Z.G. Yang, G.G. Xia, Z. Nie, J.D. Templeton

Pacific Northwest National Laboratory, Richland, WA 99352, United States

HIGHLIGHTS

- Ferritic stainless steel coated with Mn–Co spinel was tested for over 8000 h.
- The scale consisted of a chromia matrix containing regions of Mn–Cr spinel.
- Electrical resistance was lower than expected, possibly due to Ti in the scale.

ARTICLE INFO

Article history:

Received 15 October 2012

Received in revised form

3 January 2013

Accepted 5 January 2013

Available online 12 January 2013

Keywords:

Solid oxide fuel cell

Interconnect

Coatings

Electrical resistance

ABSTRACT

Long-term electrical resistance tests were performed to evaluate the performance of AISI 441 ferritic stainless steel coated with a Mn–Co spinel protection layer as a candidate material for intermediate temperature solid oxide fuel cell interconnect applications. The tests indicated that, while uncoated AISI 441 shows a substantial increase in area-specific electrical resistance (ASR), spinel-coated AISI 441 exhibits much lower ASR values. The spinel coatings reduced the oxide scale growth rate and blocked outward diffusion of Cr from the oxide scale that grew between the coating and the steel substrate during the long-term tests. The oxide scale consisted of a chromia layer containing discrete regions of Mn–Cr spinel distributed throughout the layer. The presence of Ti in the chromia scale matrix and/or the presence of regions of Mn–Cr spinel within the scale may have increased the scale electrical conductivity, which would explain the fact that the observed ASR in the tests was lower than would be expected if the scale consisted of pure chromia.

© 2013 Published by Elsevier B.V.

1. Introduction

Chromia-forming ferritic stainless steels are promising interconnect materials for intermediate temperature solid oxide fuel cell (IT-SOFC) stacks due to their relatively low cost, appropriate thermal expansion behavior, electrically conductive chromium oxide-based scale, and high temperature oxidation resistance [1–3]. However, there are several challenges associated with the use of such steels in the IT-SOFC operating environment (650–850 °C operating temperature, 40,000 h (or longer) operating lifetime, and simultaneous exposure to oxidizing and reducing environments). Specific challenges include Cr volatilization (which can degrade cathode performance) [4–7], surface instability due to oxidation and possible spallation [8–10], and increasing electrical contact resistance due to oxide scale growth at the surface [11]. Electrically conductive oxide coatings have been demonstrated to

be a promising approach for mitigating these challenges. While a number of different perovskite and spinel compositions have been evaluated as coatings [12–19], results of previous studies at PNNL demonstrated that (Mn,Co)₃O₄ spinel coatings are among the most promising candidates [20,21]. Although several (Mn,Co)₃O₄ spinel compositions were evaluated, Mn_{1.5}Co_{1.5}O₄ (hereafter designated MC) was selected as the preferred composition, due to its relatively high electrical conductivity, matching thermal expansion behavior, and the ability to mitigate both oxygen inward and chromium outward diffusion [22]. Short-term testing (up to 1000 h at 800 °C) of MC coatings on E-brite (Allegheny Ludlum, Pittsburgh, PA) and a ferritic stainless steel designed specifically for SOFC interconnect applications, Crofer22APU (ThyssenKrupp, Germany), indicated improved oxidation resistance and electrical performance compared to uncoated steel [20,23].

These results were promising, but concerns related to materials cost led to investigation of alternative, less expensive steels such as AISI 430 and AISI 441. Spinel-coated AISI 430 exhibited relatively high electrical resistance over time, probably due to formation of a continuous insulating silica sub-layer beneath the surface scale

* Corresponding author.

E-mail address: jeff.stevenson@pnnl.gov (J.W. Stevenson).

(due to the relatively high residual Si content in the steel) [22]. On the other hand, although AISI 441 also exhibited some silicon diffusion to the scale/steel interface, no continuous silica sub-layer formation was observed, likely due to the growth of Si-rich Laves phases within the bulk of the steel that reduced transport of Si to the surface [24,25]. As a result, when AISI 441 was coated with MC spinel, low electrical resistance was maintained over a relatively long time frame [25]. Specifically, while the area-specific resistance (ASR) for uncoated AISI 441 after 5500 h at 800 °C was ~ 60 mOhm cm² (and still rising steadily), the ASR for the MC-coated AISI 441 was only ~ 13 mOhm cm² (and nearly stable over time).

As native oxide scales grow thicker over time at SOFC operating temperatures, the interface between the scale and the underlying steel substrate can become a weak link that leads to surface instability and high electrical resistance due to buckling or spallation of the scale from the substrate. This is more likely to be an issue in steels, such as AISI 441, that do not contain any rare earth element additions. The alloying of a small amount of rare earths into chromia-forming steel is a well-established way to improve the scale adhesion [26], but these additions tend to increase the cost of the steel. Alternatively, small additions of a rare earth (e.g., Ce) to MC coating materials were determined to be a means of achieving improved scale adhesion without the need for rare earths to be added to the steel itself [27]. Based on these results, spinel-coated AISI 441 was determined to be an excellent candidate for further long-term evaluation as a potential interconnect material for IT-SOFC stacks. Results of long-term tests are summarized in this paper.

2. Experimental

The AISI 441 ferritic stainless steel, manufactured by Allegheny Ludlum, Inc. (Pittsburgh, PA), had a chemical composition (in wt %) of 17.6% Cr, 0.33% Mn, 0.47% Si, 0.46% Nb, 0.18% Ti, 0.20% Ni, 0.01% C, 0.045% Al, 0.024% P, 0.001% S, with Fe as the balance. Steel sheet with a thickness of 1.5 mm was cut into 25.4 × 12.7 mm coupons. The coupons were hand polished with 1200 grit abrasive paper, cleaned in an ultrasonic acetone bath for 5 min, and then rinsed with 2-propanol prior to application of the coatings.

Mn_{1.5}Co_{1.5}O₄ and Mn_{1.475}Co_{1.475}Ce_{0.05}O₄ powders were prepared using the glycine-nitrate combustion synthesis method [28]. The powders were ball milled and then mixed with a binder solution to form a slurry that was applied to the steel coupons via screen-printing. The coated samples were heat-treated in a reducing environment (2.75% H₂ + 3% H₂O + 94.25% Ar) for 2 h and then oxidized in ambient air at 800 °C for 1 h. The electrical resistance of coated and uncoated steel coupons was measured at 800 °C in air using a four probe dc technique. For the electrical resistance tests, (La_{0.8}Sr_{0.2})_{0.98}MnO₃ (LSM-20) contact paste was applied to an LSM-20 pellet which was then placed between two coated steel coupons. Pt wires were spot-welded to the coupons. During the test, a constant current density of 500 mA cm⁻² was applied to the coupons through two Pt current leads, while the voltage drop across the two alloy coupons was measured with two Pt voltage leads.

Once the ASR tests were completed, the samples were epoxy-mounted, sectioned, and polished. Cross sections of the samples were analyzed using a JEOL scanning electron microscope. Compositional analysis was conducted using an Oxford INCA energy dispersive spectrometer system (EDS). X-ray elemental mapping and point analyses were conducted at 20 keV to determine elemental distributions using K_α (Ti, Cr, Mn, Fe, Co, Al, Si) and L_α (Nb) radiation. Crystallographic information regarding specific crystal structures present in the oxide scale that formed between the coating and steel substrate during the ASR tests was obtained using an HKL Channel 5 electron backscatter diffraction (EBSD) system

equipped with a Nordlys CCD camera. The samples were carbon coated and tilted to 70° for the EBSD analysis.

3. Results and discussion

Fig. 1 summarizes results from long-term (8844 h) ASR measurements performed in air at 800 °C. Results from three tests are shown: bare (uncoated) AISI 441, AISI 441 coated with Mn_{1.5}Co_{1.5}O₄ (MC), and AISI 441 coated with Mn_{1.475}Co_{1.475}Ce_{0.05}O₄ (Ce-MC). It should be noted that, although for convenience the Ce-doped composition is written as a single phase spinel, most of the Ce was actually present in the form of fine, dispersed ceria particles throughout the coating matrix, due to the limited solubility of Ce in Mn_{1.5}Co_{1.5}O₄ [27].

It is clear from Fig. 1 that the uncoated AISI 441 showed a substantial increase in ASR during the test (to a final ASR value of ~ 75 mOhm cm²). On the other hand, the AISI 441 coated with MC or Ce-MC spinel exhibited much greater stability, with both samples exhibiting similar final ASR values in the range of only 11–13 mOhm cm². It should be noted that the large discontinuities in the ASR plot for the uncoated AISI 441 correlate with several unscheduled facility power outages which resulted in rapid cooling of the samples from the test temperature (800 °C) to near room temperature.

Once the ASR tests were complete, the samples were cooled and then dis-assembled for post-test characterization. SEM/EDS analysis was performed on polished cross-sections of the tested samples. Representative post-test cross-section microstructures for MC AISI 441, Ce-MC AISI 441, and uncoated AISI 441 are shown in Figs. 2–4, respectively. In Fig. 2, from left to right, the components are AISI 441 substrate, oxide scale (which developed during the ASR test), MC spinel coating, LSM contact paste, and the LSM simulated cathode. Note that the simulated cathode consisted of a porous layer of LSM (to simulate a cathode microstructure) fabricated onto a denser LSM pellet (to provide structural integrity during the test). Figs. 3 and 4 are similarly structured, except that Fig. 3 includes a Ce-MC spinel coating instead of an MC spinel coating, and there is no coating present in Fig. 4.

Examination of Figs. 2–4 reveals a difference in the thickness of the oxide scale that grew on the steel substrate during the test. Average scale thicknesses for the uncoated AISI 441, MC spinel-coated AISI 441, and Ce-MC spinel coated AISI 441 were approximately 10, 5, and 4 microns, respectively. The reduced scale thickness for the coated samples is consistent with previous short

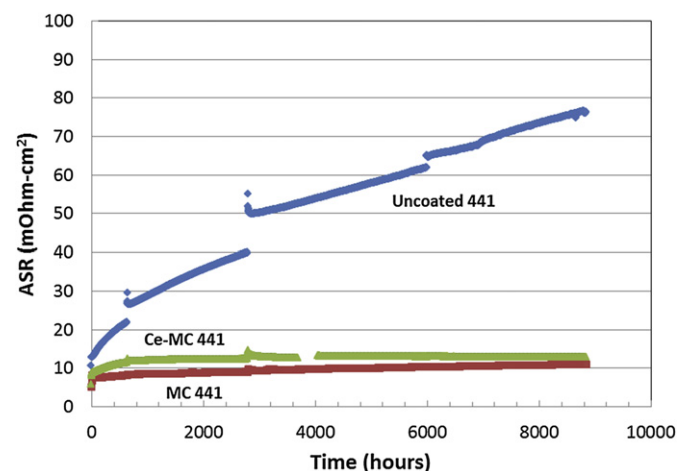


Fig. 1. Area-specific electrical resistance (ASR) for AISI 441 with and without a protective spinel coating. Test was performed in air at 800 °C.

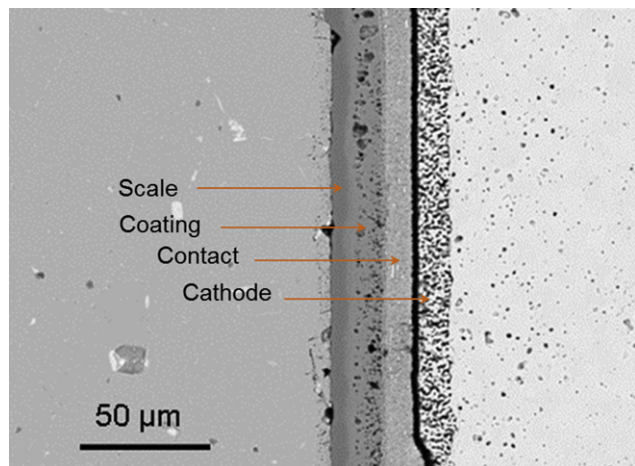


Fig. 2. Cross-sectional SEM micrograph of MC spinel-coated AISI 441 after long-term ASR test at 800 °C in air.

term studies, which also observed slower oxidation rates for MC spinel-coated AISI 441 compared to uncoated AISI 441 at 800 °C [25]. Scale formation requires the presence of oxygen to react with elements (primarily Cr) in the steel, so it is not surprising that the presence of the coating on the surface of the steel would reduce the amount of oxygen available for oxide formation, thereby reducing the scale growth rate. It will also be noted that the scale that grew beneath the Ce-modified MC spinel coatings was somewhat thinner than the scale beneath the Ce-free MC spinel coating. This is consistent with previous studies on the effect of Ce and other rare earth elements on the oxidation behavior of chromia-forming alloys [26]. It should also be noted that spallation of the oxide scale from the underlying steel substrate was observed on the uncoated back sides of the tested coupons (the coupons were only coated on one side). These results are consistent with previous studies regarding the ability of MC spinel coatings to reduce scale growth rates, and delay onset of spallation [27], as no scale spallation was observed on the coated sides of the tested coupons.

As noted in the [Introduction](#), a previous study indicated that the addition of Ce to MC spinel coatings resulted in improved scale adhesion, as evidenced by the presence of microscopic gaps at the scale/AISI 441 interface in samples coated with Ce-free MC spinel [27]. These gaps, which were much more obvious after testing at 850 °C than at 800 °C, were believed to have formed during cooling

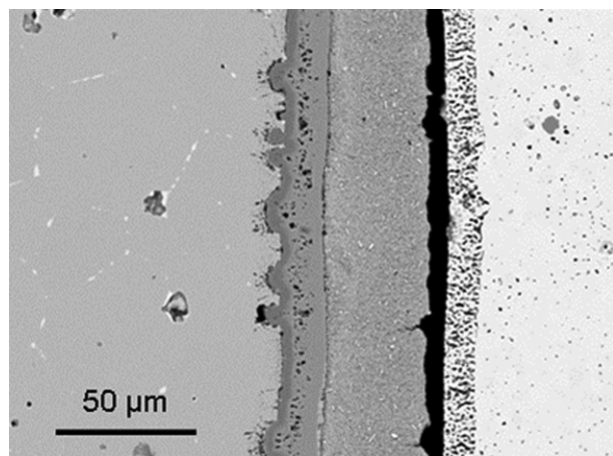


Fig. 3. Cross-sectional SEM micrograph of Ce-MC spinel coated AISI 441 after long-term ASR test at 800 °C in air.

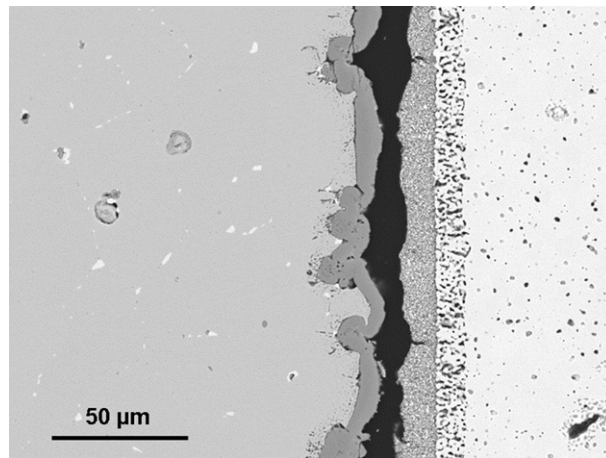


Fig. 4. Cross-sectional SEM micrograph of uncoated AISI 441 after long-term ASR test at 800 °C in air.

or during metallographic preparation, as no significant difference in ASR was observed during 700–1000 h of ASR testing. Similarly, in the present study, the long-term ASR measurements at 800 °C indicated similar ASR values regardless of whether or not the spinel coating contained Ce. Also, no microscopic cracks or gaps were observed at the scale/AISI 441 interface for either the sample coated with Ce-free MC spinel or the sample coated with Ce-containing spinel. Based on the previously reported results, it is likely that a difference in behavior would have been observed had the testing been performed at 850 °C.

The presence or absence of Ce in the MC spinel coating did result in a difference in the scale/alloy interfacial morphology. The interface was relatively smooth in the AISI 441 coated with Ce-free MC spinel (Fig. 2), while the interface was much more irregular in the AISI 441 coated the Ce-modified MC spinel (Fig. 3). Note that an irregular interface also formed in the uncoated AISI 441 (Fig. 4). The mechanism behind this difference in behavior is not known, although the irregular interface clearly correlates with the presence of a rare earth element (i.e., Ce in the coating in Fig. 3; La in the LSM contact material in Fig. 4).

In the spinel-coated samples, de-bonding was observed at the interface between the LSM contact material and the LSM simulated cathode, indicating that stronger bonding occurred between the contact material and the coating material, the coating material and the oxide scale, and the oxide scale and the steel substrate. Given the thermal cycle stability and low magnitude of the measured ASRs for those samples, it is likely that the de-bonding at the contact/cathode interface of those samples did not occur until the samples were being prepared for post-test SEM analysis. On the other hand, for the uncoated sample, de-bonding occurred at the interface between the contact material and the oxide scale, which was only present in the uncoated sample. This result, which indicates that the contact/scale interface was weaker than the contact/cathode interface, is consistent with the ASR results in Fig. 1. As noted above, significant discontinuities in ASR occurred during unscheduled thermal cycling of the uncoated sample. These may have been caused by reduction of electrical contact due to local failures of the bonding at the contact/scale interface. As noted above, the other two samples, in which this interface was not present, exhibited only minor disruptions in ASR during the thermal cycles.

Fig. 5 shows a representative SEM cross section of the post-test MC spinel-coated AISI 441 on which a series of EDS point scan analyses were performed; results of the point scans are listed in Table 1. Cross-sectional EDS analyses on the post-test Ce-MC spinel-coated

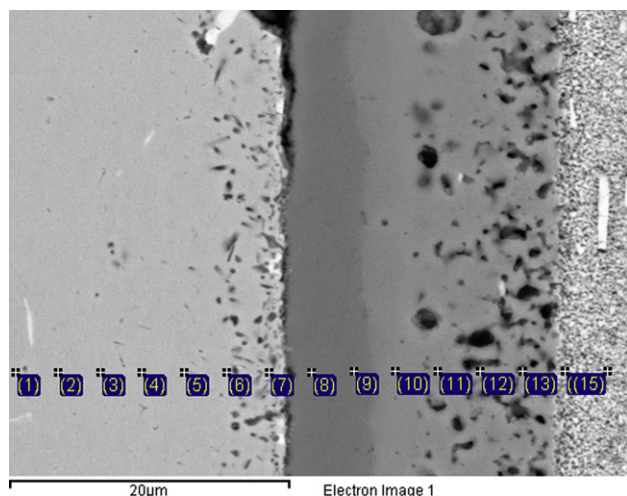


Fig. 5. Representative SEM cross section of the post-test MC spinel-coated AISI 441 on which a series of EDS point scan analyses were performed; results of the numbered point scans are listed in Table 1.

AISI 441 yielded similar results to those shown in Table 1. As expected, the oxide scales that grew between the steel substrate and the coating were rich in Cr, with a substantial amount of Mn also present. Previously, short-term tests (500–1000 h) led to formation of scales in which the Mn content was higher in the outer layer of the scale [25]. This was consistent with the oxidation behavior of uncoated ferritic stainless steels, which typically form a dual layer scale consisting of a $(\text{Mn,Cr})_3\text{O}_4$ spinel-rich top layer and a chromia sub-layer [11]. In these long-term samples, however, the dual layer structure did not appear to be as pronounced; the scale structure and chemistry will be discussed in more detail below. While there was some evidence of Cr diffusion into the coating near the coating/scale interface, the EDS analyses found no evidence of Cr migration through the coating or into the LSM contact material, indicating that the desirable Cr blocking behavior observed during previous short-term tests could be sustained during long term testing as well. It was also noted that the Mn to Co ratio was higher than the initial 1 to 1 ratio in the spinel coating material (e.g., $\text{Mn}_{1.5}\text{Co}_{1.5}\text{O}_4$), due to diffusion of Mn into the coating from the AISI 441 and LSM contact material, and/or diffusion of Co from the coating into the LSM contact material. Note that some Co was detected in the contact material near the coating/contact material interface.

The EDS analysis also revealed the presence of Fe in the spinel coating. It is likely that the Fe was incorporated into the coating

during the early stages of oxide film formation before a fully dense, protective chromia scale was formed. It is interesting to note that a recent study found that pre-oxidation of AISI 441 prior to application of an MnCo coating significantly reduced the amount of Fe detected in the coating after 1650 h of oxidation at 800 °C, probably due to the rapid formation of an iron-blocking protective chromia scale during the pre-oxidation step [29]. In another recent study, after testing at 800 °C for 850 h, no Fe was detected in coatings fabricated onto AISI 441 from electrodeposited MnCo alloys, suggesting that the method of fabricating the coating may influence subsequent oxidation behavior and diffusion of elements from the steel [30].

During ASR testing, the measured ASR included resistance contributions from all of the constituents making up the sample: AISI 441 steel, oxide scale, spinel coating, contact material (LSM), and cathode material (also LSM). It should be noted that the electrical conductivity of oxides can be highly dependent on subtle changes in dopant/impurity level and oxygen stoichiometry. However, due to their high intrinsic conductivities relative to that of chromium oxide, it is likely that the resistances of the steel, spinel coating, and LSM provided a negligible contribution to the total sample resistance. Thus, it seems appropriate to assume that the resistance measured in the test was due almost exclusively to the resistance of the oxide scale that grew between the alloy substrate and the coating. The ASR of the MC spinel-coated AISI 441 sample after 8844 h at 800 °C was $\sim 11 \text{ m}\Omega\text{cm}^2$. The average thickness of the scale was ~ 5 microns, which yielded a calculated conductivity for the scale of $\sim 0.045 \text{ S cm}^{-1}$. The ASR of the Ce-MC spinel-coated AISI 441 sample was $\sim 13 \text{ m}\Omega\text{cm}^2$. The average thickness of the scale was ~ 4 microns, yielding a similar calculated conductivity for the scale of $\sim 0.031 \text{ S cm}^{-1}$. It can be noted that, if chemical interactions led to any interfacial reaction zones which contributed significantly to the measured ASR, this would require that the conductivity of the oxide scale be even higher than these values, as, in that case, the scale would not be the only non-negligible source of electrical resistance in the sample.

Obviously, the composition and structure of the oxide scale determines its electrical properties. The conductivity of chromia, Cr_2O_3 , at 800 °C is $\sim 0.02 \text{ S cm}^{-1}$ [31], so, if the scale was composed of pure chromia a scale thickness of 5 microns should have yielded an ASR of $\sim 25 \text{ m}\Omega\text{cm}^2$, which is more than double the measured value at the end of the long-term tests. This suggested that the

Table 1

EDS spectra for the points indicated in Fig. 5 (MC spinel-coated AISI 441). Results are in atomic %.

Spectrum	Al	Si	Ti	Cr	Mn	Fe	Co	Sr	La
(1)		1.1		18.3		80.6			
(2)		1.1		18.6		80.2			
(3)		1.1		18.7		80.2			
(4)		1.1		18.8		80.1			
(5)		1.4		18.5		80.1			
(6)	1.5	1.3		18.6		78.6			
(7)	6.3		2.8	17.4		65.8			
(8)			1.1	61.8					
(9)			0.9	60.8					
(10)			1.0	8.7	30.0	2.6	25.4		
(11)			1.2	1.2	39.3	2.97	23.2		
(12)			1.2	0.6	39.7	2.45	23.0		
(13)			1.0	0.7	45.6	3.04	25.9		
(14)					34.3	2.06	8.2	5.4	23.1
(15)					32.3		3.5	6.4	29.2

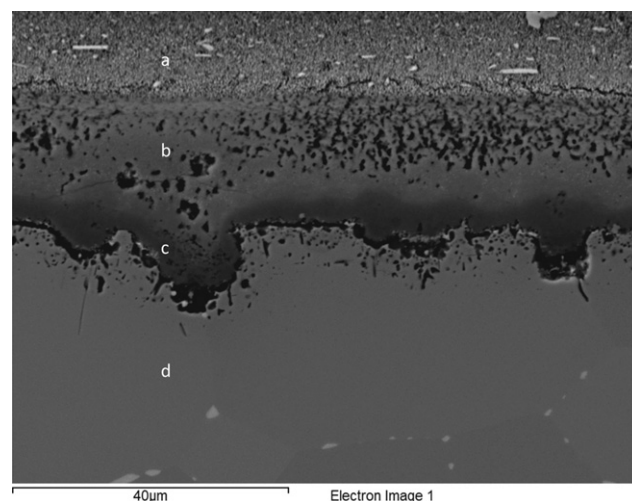


Fig. 6. SEM image of a representative cross-section of the post-test Ce-MC spinel-coated AISI 441 sample; the components from top to bottom are a) LSM contact material, b) spinel coating, c) oxide scale, and d) steel substrate.

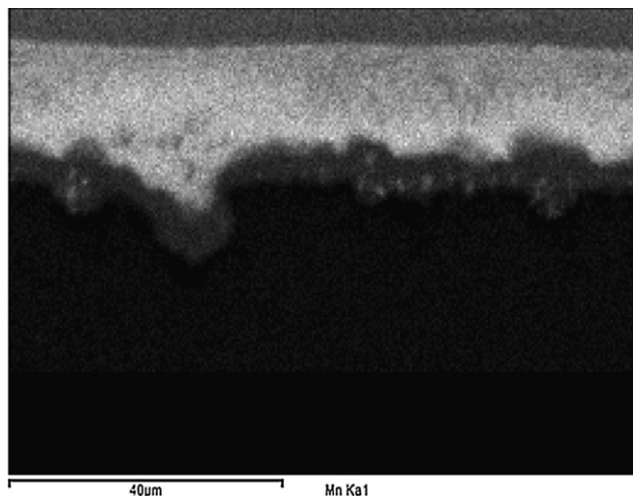


Fig. 7. SEM/EDS elemental dot map for manganese (same cross-section region as shown in Fig. 6).

oxide scale that grew between the coating and the steel substrate was not pure chromia. Therefore, additional analysis was performed on the post-test Ce-MC spinel-coated AISI 441 sample in order to obtain a deeper understanding of the composition and structure of the oxide scale.

Fig. 6 shows an SEM image of a representative cross-section of the post-test Ce-MC spinel-coated AISI 441 sample; the components from top to bottom are LSM contact material, spinel coating, oxide scale, and steel substrate. Fig. 7–12 show elemental dot maps of the same region for manganese, chromium, titanium, cobalt, niobium, and silicon, respectively. These figures indicate that the oxide scale consisted of a Cr rich oxide layer in which some regions contained an enhanced amount of Mn. The apparent lack of Cr in the coating (see Fig. 8) is consistent with quantitative EDS analyses (e.g., Table 1) that detected minimal (~1 atomic % or less) Cr content in the spinel coatings. To obtain structural information regarding the scale, EBSD analysis was performed on selected regions of the scale. EBSD results on locations in the Cr rich oxide layer indicated a hexagonal corundum structure, consistent with a typical chromia scale. EBSD results from one such analysis are shown in Fig. 13; note the excellent agreement between the

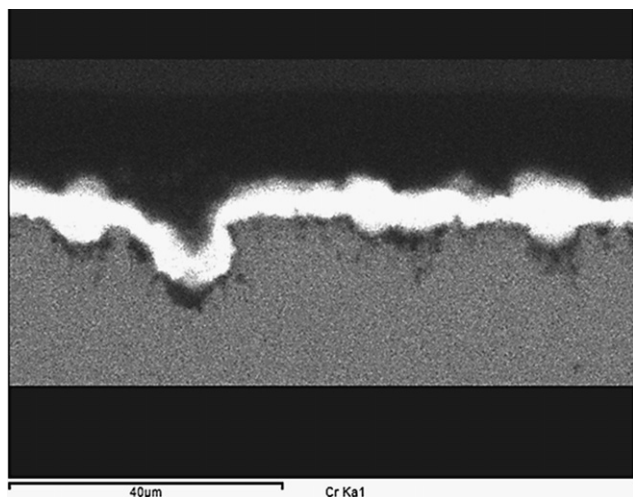


Fig. 8. SEM/EDS elemental dot map for chromium (same cross-section region as shown in Fig. 6).

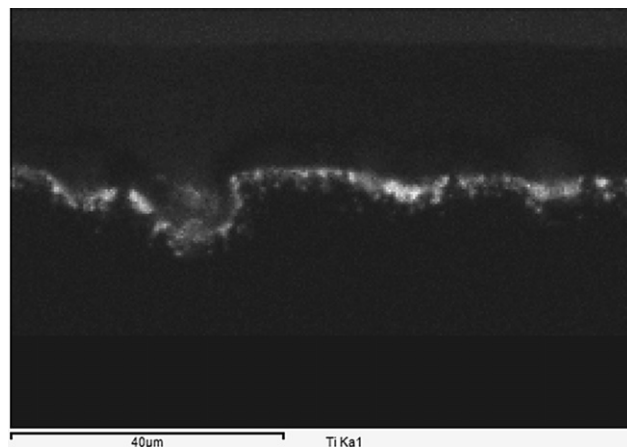


Fig. 9. SEM/EDS elemental dot map for titanium (same cross-section region as shown in Fig. 6).

sample's diffraction pattern (Fig. 13a) and the reference pattern (superimposed on the sample diffraction pattern in Fig. 13b). EBSD analysis on Mn-enhanced regions within the chromia scale indicated a cubic spinel structure. EBSD results from one such analysis are shown in Fig. 14; again, note the excellent agreement between the sample's diffraction pattern and reference pattern. EDS results on that spot indicated a composition (atomic %) of 26% Cr, 5% Mn, 4% Ti, 2% Fe, 1% Si, balance O. As noted above, Mn–Cr spinel was previously observed as a component of the oxide scale formed above ferritic stainless steels, although in those shorter term studies, the Mn–Cr spinel phase was reported to be primarily present as a top layer of the scale, rather than being dispersed throughout the scale matrix, as appears to be the case in the present study.

Although it was clear that some of the residual silicon present in the AISI 441 diffused to the scale/steel interface, the low ASR values observed during the long term ASR tests indicate that either the silicon-rich regions did not consist of insulating silica or, if they did, that those regions did not form a continuous layer across the interface.

Titanium (originally present as a minor alloying element in the AISI 441 steel) was observed to be concentrated primarily in oxide

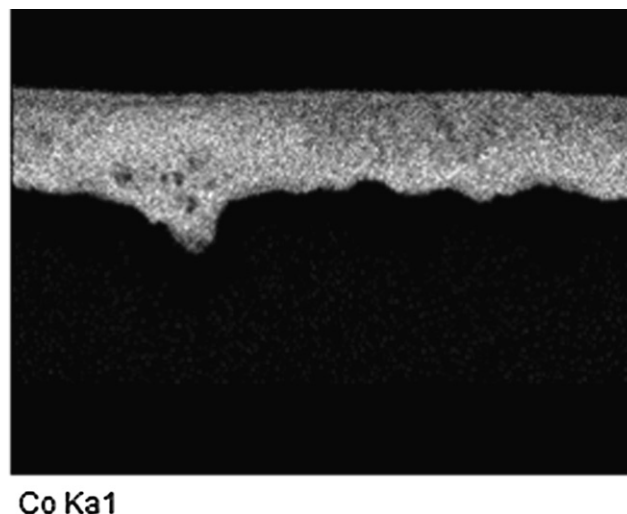
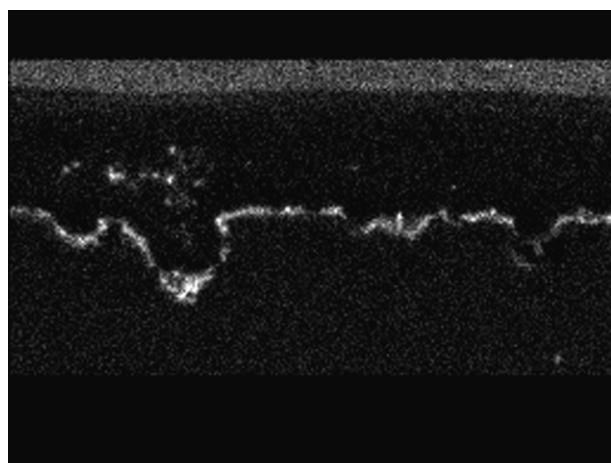


Fig. 10. SEM/EDS elemental dot map for cobalt (same cross-section region as shown in Fig. 6).



Nb La1

Fig. 11. SEM/EDS elemental dot map for niobium (same cross-section region as shown in Fig. 6).

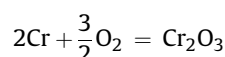


Si Ka1

Fig. 12. SEM/EDS elemental dot map for silicon (same cross-section region as shown in Fig. 6).

precipitates between the scale and the steel substrate, but EDS analysis also indicated that some Ti was present in the oxide scale itself. EDS point scan analysis was used to quantitatively determine the amount of Ti present in the chromia scale. The results, summarized in Fig. 15 and Table 2, indicate that the Ti content in the scale was in the range of 0.5–0.7 atomic %.

Given the presence of Ti in the chromia-based scale, it was of interest to evaluate the possible impact of that Ti on the electrical conductivity of the scale. Holt and Kofstad [32] evaluated the electrical behavior of chromia doped with 2% Ti, which is somewhat higher than, but similar to, the Ti content observed in the chromia scale in the present study. They concluded that, at high oxygen activity, the Ti donor ions were compensated by chromium vacancies rather than electrons. This conclusion is consistent with the rather low, p-type conductivity they observed for Ti-doped chromia at high oxygen activity (e.g., air). On the other hand, the Ti-doped chromia exhibited much higher electrical conductivity at low oxygen activities (e.g., $\sim 0.2 \text{ S cm}^{-1}$ at 1000°C at 10^{-18} atm). While the specifics of the oxygen activity gradient across the scale of the sample in the present study are not known, two boundary conditions are known (see Fig. 16). The oxygen activity at the coating/porous contact material interface should correspond to that of air ($10^{-0.7}$ atm). The oxygen activity at the scale/alloy interface should correspond to the oxygen activity in equilibrium with the Cr in the alloy and the Cr_2O_3 scale. This can be calculated from the formation reaction for Cr_2O_3 :



The free energy for the above reaction at 800°C is -849 kJ mol^{-1} , so the equilibrium constant is 2.14×10^{41} :

$$K = 2.14 \times 10^{41} = \frac{a_{\text{Cr}_2\text{O}_3}}{a_{\text{Cr}}^2 a_{\text{O}_2}^{1.5}}$$

Substitution of activities for Cr_2O_3 and Cr (assumed to be 1.00 and 0.18, respectively; note that the steel contains $\sim 18\%$ Cr) [33] yields an oxygen activity of 2.7×10^{-27} atm at the scale/alloy interface. The oxygen activity at the other side of the scale (i.e., at the coating/scale interface) is not known. However, given the fact that the coating appeared to be sufficiently dense to be impermeable to molecular oxygen, it seems plausible to assume that the oxygen activity at that interface was much lower than the oxygen activity at the coating/porous contact interface (PO_2 of air = $10^{-0.7}$ atm), which would impose a relatively low oxygen activity across the thickness of the scale. Thus, it is possible that this low oxygen activity across the Ti-containing chromia scale led to an increase in the scale's electrical conductivity (similar to that observed by Holt and Kofstad), which would account for the unexpectedly low magnitude of ASR observed during the test.

The dispersed regions of Mn–Cr spinel within the scale may also have contributed to an increase in the overall scale conductivity. The electrical conductivity of MnCr_2O_4 is 0.003 S cm^{-1} at 800°C , while the conductivity of $\text{Mn}_{1.5}\text{Cr}_{1.5}\text{O}_4$ is 0.07 S cm^{-1} at 800°C [34]. Thus, if the composition of the Mn–Cr spinel in the scale tended toward the later stoichiometry, the conductivity of

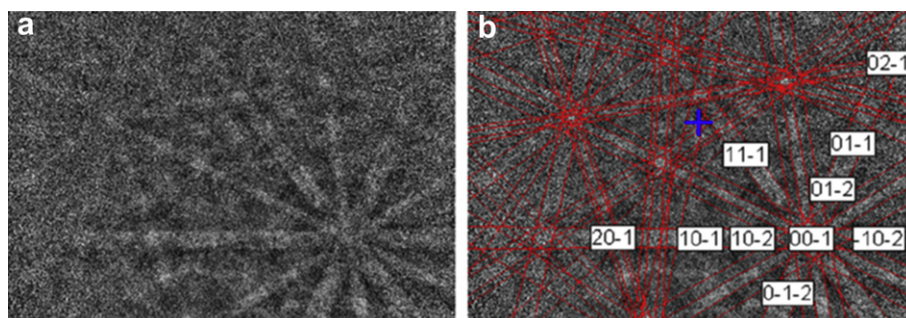


Fig. 13. EBSD analysis on representative region of Cr-rich oxide scale: a) sample diffraction pattern; b) reference pattern superimposed on sample diffraction pattern.

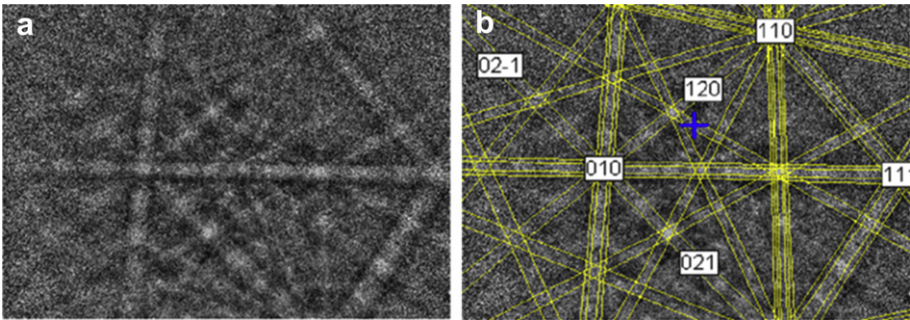


Fig. 14. EBSD analysis on representative Mn-enhanced region within the chromia scale: a) sample diffraction pattern; b) reference pattern superimposed on sample diffraction pattern.

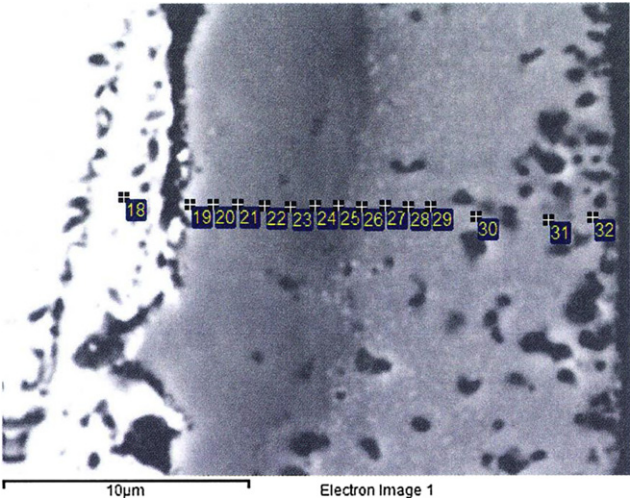


Fig. 15. Representative SEM cross section of the post-test Ce-MC spinel-coated AISI 441 on which a series of EDS point scan analyses were performed; results of the numbered point scans are listed in Table 2.

that phase could have equaled or exceeded the experimentally determined conductivity of the composite (chromia plus Mn–Cr spinel) scale ($0.03\text{--}0.05\text{ S cm}^{-1}$). As noted above, in shorter term tests the Mn–Cr spinel was observed to be present as a top layer in the oxide scale [25]. The reason for this apparent change in scale structure over time is not clear, but the results in the present study clearly indicate that this change did not adversely affect the electrical performance of the spinel-coated AISI 441 steel over the time

Table 2
EDS spectra for the points indicated in Fig. 15 (Ce-MC spinel-coated AISI 441). Results are in atomic %.

Spectrum	Al	Si	Ti	Cr	Mn	Fe	Co	Nb	Ce
18	0.9	1.2	1.8	19.1		77.0			
19		1.6	1.0	28.5	0.5	3.3		0.7	
20			0.6	32.2	3.8	0.5			
21			0.6	34.8		0.2			
22			0.6	35.9		0.2			
23			0.6	37.4		0.2			
24			0.5	38.8		0.3	2.0		
25			0.5	34.4	3.7	0.9	6.6		
26			0.5	11.1	17.1	4.8	14.9		0.6
27			0.7	1.5	22.2	6.1	16.1		0.7
28			0.7	0.8	22.7	6.2	15.7		0.6
29			0.7	0.6	21.9	6.1	15.3		0.5
30		2.5	0.6	0.5	20.5	5.7	14.6		0.7
31			0.6	0.2	21.2	5.8	15.3		0.6
32			0.5	0.2	21.1	5.8	15.4		0.5

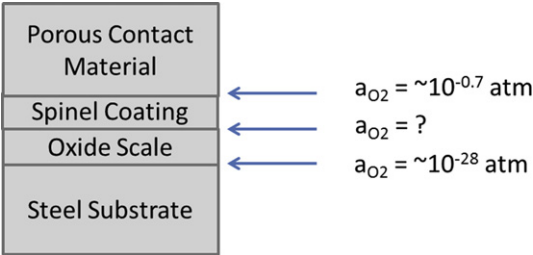


Fig. 16. Schematic illustration of the oxygen activity “boundary conditions” at various interfaces.

frame of the study (8844 h). It is possible, however, that continuing changes in the scale thickness, structure, and chemistry would lead to higher ASR values for exposure times greater than 8844 h; this possibility is of interest given the fact that a typical operating lifetime target for an SOFC stack is considerably longer than 8000 h (e.g., 40,000 h or more).

4. Conclusions

Long-term tests (8844 h) confirmed that spinel-coated AISI 441 steel is a promising candidate material system for IT-SOFC interconnect applications. While uncoated AISI 441 showed a substantial increase in ASR during the test (to a final ASR value of $\sim 75\text{ mOhm cm}^2$), AISI 441 coated with MC or Ce-MC spinel exhibited much lower ASR values in the range of only 11–13 mOhm cm^2 . Consistent with previous shorter term tests, formation of a continuous insulating silica sublayer beneath the native chromia-based scale was not observed, and the spinel coatings reduced the oxide scale growth rate and blocked outward diffusion of Cr from the scale. The ASR values observed for the coated AISI 441 were lower than would be expected if the oxide scale was comprised of pure chromium oxide, and, indeed, SEM/EDS analyses confirmed that the scale grown during the long term tests was not pure chromium oxide. Instead, it consisted of a chromia layer containing discrete regions of Mn–Cr spinel distributed throughout the layer. The presence of a small percentage of Ti in the chromia scale matrix and/or the presence of regions of Mn–Cr spinel within the scale may have resulted in increased scale electrical conductivity, which would explain the anomalously low ASR values observed in the tests on spinel-coated AISI 441.

Acknowledgments

The authors would like to thank Jim Rakowski at Allegheny Technologies, Inc. for providing the alloy samples, and Dan Edwards and Jim Coleman at PNNL for performing the SEM/EDS analyses.

The work summarized in this paper was funded by the U.S. Department of Energy's Solid-State Energy Conversion Alliance (SECA) Core Technology Program. PNNL is operated by Battelle Memorial Institute for the U.S. Department of Energy under Contract DE-AC06-76RLO 1830.

References

- [1] J.W. Fergus, *Mater. Sci. Eng. A* 397 (2005) 271–283.
- [2] Z.G. Yang, K.S. Weil, D.M. Paxton, J.W. Stevenson, *J. Electrochem. Soc.* 150 (2003) A1188–A1201.
- [3] J.W. Wu, X.B. Liu, *J. Mater. Sci. Technol.* 26 (2010) 293–305.
- [4] C. Gindorf, L. Singheiser, K. Hilpert, *Steel Res.* 72 (2001) 528–533.
- [5] C. Gindorf, L. Singheiser, K. Hilpert, M. Schroeder, M. Martin, H. Greiner, F. Richter, *Chromium Vaporization from Metallic Interconnect and Retention by Perovskite Layers*, Electrochemical Society Inc, Pennington, 1999.
- [6] K. Hilpert, D. Das, M. Miller, D.H. Peck, R. Weiss, *J. Electrochem. Soc.* 143 (1996) 3642–3647.
- [7] C. Sun, R. Hui, J. Roller, *J. Solid State Electrochem.* 14 (2010) 1125–1144.
- [8] Z.G. Yang, M.S. Walker, P. Singh, J.W. Stevenson, *Electrochem. Solid State Lett.* 6 (2003) B35–B37.
- [9] Z.G. Yang, M.S. Walker, P. Singh, J.W. Stevenson, T. Norby, *J. Electrochem. Soc.* 151 (2004) B669–B678.
- [10] Z.G. Yang, G.G. Xia, M.S. Walker, C.M. Wang, J.W. Stevenson, P. Singh, *Int. J. Hydrogen Energy* 32 (2007) 3770–3777.
- [11] Z.G. Yang, J.S. Hardy, M.S. Walker, G.G. Xia, S.P. Simner, J.W. Stevenson, *J. Electrochem. Soc.* 151 (2004) A1825–A1831.
- [12] S. Linderth, *Surf. Coat. Technol.* 80 (1996) 185–189.
- [13] T. Kadowaki, T. Shiomitsu, E. Matsuda, H. Nakagawa, H. Tsuneizumi, T. Maruyama, *Solid State Ion.* 67 (1993) 65–69.
- [14] W.J. Quadackers, H. Greiner, M. Hansel, A. Pattanaik, A.S. Khanna, W. Mallener, *Solid State Ion.* 91 (1996) 55–67.
- [15] K. Fujita, K. Ogasawara, Y. Matsuzaki, T. Sakurai, *J. Power Sources* 131 (2004) 261–269.
- [16] S. Elangovan, S. Balagopal, U. Timper, L. Bay, D. Larsen, J. Hartvigsen, *J. Mater. Eng. Perform.* 13 (2004) 265–273.
- [17] Y. Larring, T. Norby, *J. Electrochem. Soc.* 147 (2000) 3251–3256.
- [18] Z.G. Yang, G.G. Xia, G.D. Maupin, J.W. Stevenson, *J. Electrochem. Soc.* 153 (2006) A1852–A1858.
- [19] N. Shaigan, W. Qu, D.G. Ivey, W. Chen, *J. Power Sources* 195 (2010) 1529–1542.
- [20] Z.G. Yang, G.G. Xia, G.D. Maupin, J.W. Stevenson, *Surf. Coat. Technol.* 201 (2006) 4476–4483.
- [21] Z.G. Yang, G.G. Xia, S.P. Simner, J.W. Stevenson, *J. Electrochem. Soc.* 152 (2005) A1896–A1901.
- [22] Z.G. Yang, G.G. Xia, X.H. Li, J.W. Stevenson, *Int. J. Hydrogen Energy* 32 (2007) 3648–3654.
- [23] Z.G. Yang, G.G. Xia, J.W. Stevenson, *Electrochem. Solid State Lett.* 8 (2005) A168–A170.
- [24] D. Dulieu, J. Cotton, H. Greiner, K. Honegger, A. Scholten, T. Seguelong, in: P. Stevens (Ed.), *Third European SOFC Forum, European Solid Oxide Fuel Cell Forum*, Geneva, Switzerland (1998), p. 447.
- [25] Z.G. Yang, G.G. Xia, C.M. Wang, Z.M. Nie, J. Templeton, J.W. Stevenson, P. Singh, *J. Power Sources* 183 (2008) 660–667.
- [26] P. Kofstad, *High Temperature Corrosion*, Elsevier Applied Science Publishers, Essex, England, 1988.
- [27] Z.G. Yang, G.G. Xia, Z.M. Nie, J. Templeton, J.W. Stevenson, *Electrochem. Solid State Lett.* 11 (2008) B140–B143.
- [28] L.A. Chick, L.R. Pederson, G.D. Maupin, J.L. Bates, L.E. Thomas, G.J. Exarhos, *Mater. Lett.* 10 (1990) 6–12.
- [29] K.O. Hoyt, P.E. Gannon, P. White, R. Tortop, B.J. Ellingwood, H. Khoshuei, *Int. J. Hydrogen Energy* 37 (2012) 518–529.
- [30] J. Wu, R.S. Gemmen, A. Manivannan, X. Liu, *Int. J. Hydrogen Energy* 36 (2011) 4525–4529.
- [31] W.C. Hagel, A.U. Seybolt, *J. Electrochem. Soc.* 108 (1961) 1146–1152.
- [32] A. Holt, P. Kofstad, *Solid State Ion.* 117 (1999) 21–25.
- [33] N. Birks, G.H. Meier, F.S. Pettit, *Introduction to the High-Temperature Oxidation of Metals*, second ed., Cambridge University Press, Cambridge, U.K, 2006.
- [34] A. Petric, H. Ling, *J. Am. Ceram. Soc.* 90 (2007) 1515–1520.